

A Data-Driven Methodology for Probabilistic Wind Power Ramp Forecasting

Mingjian Cui, *Member, IEEE*, Jie Zhang, *Senior Member, IEEE*, Qin Wang, *Member, IEEE*, Venkat Krishnan, *Member, IEEE*, and Bri-Mathias Hodge, *Senior Member, IEEE*

Abstract—With increasing wind penetration, wind power ramps (WPRs) are currently drawing great attention to balancing authorities, since these wind ramps largely affect power system operations. To help better manage and dispatch the wind power, this paper develops a data-driven probabilistic wind power ramp forecasting (p-WPRF) method based on a large number of simulated scenarios. A machine learning technique is first adopted to forecast the basic wind power forecasting scenario and produce the historical forecasting errors. To accurately model the distribution of wind power forecasting errors (WPFEs), a generalized Gaussian mixture model (GGMM) is developed and the cumulative distribution function (CDF) is also analytically deduced. The inverse transform method based on the CDF is used to generate a large number of forecasting error scenarios. An optimized swinging door algorithm (OpSDA) is adopted to extract all the WPRs from the complete set of wind power forecasting scenarios. The p-WPRF is generated based on all generated scenarios under different weather and time conditions. Numerical simulations on publicly available wind power data show that the developed p-WPRF method can predict WPRs with a high level of reliability and accuracy.

Index Terms—Gaussian mixture model, probabilistic wind power ramp forecasting, scenario generation, wind power ramps.

NOMENCLATURE

A. Sets, Parameters, Variables, and Functions:

$\text{cov}(\cdot)$	Covariance function.
$\text{erf}(\cdot)$	Gaussian error function.
$f(\cdot), F(\cdot)$	PDF and CDF of the GGMM.
$g_i(\cdot)$	Probability distribution function of the i th Gaussian model.
h	Predefined parameter to obtain the constant in the GGMM CDF.
i, \mathcal{G}, N_G	Index, set, and total number of Gaussian models.
j, \mathcal{X}, N_X	Index, set, and total number of WPFEs.
k	Iteration number.
m, n, v, t	Index of time periods in the forecasting horizon. $m, n, v, t=1, 2, 3, \dots, T_{\text{fh}}$.
r, z	Random number.
s, N_{sc}	Index and total number of forecasting scenarios.
x_j, p_j	The j th actual WPFE and its actual probability.
\hat{x}	Sampled random WPFE.
y_t, \hat{y}_t	Measured value and deterministic forecasting value of wind power at time t .
ACE	Average coverage error.
AIS	Average interval score.

M. Cui and J. Zhang are with the Department of Mechanical Engineering, the University of Texas at Dallas, Richardson, TX 75080, USA, e-mail: ({mingjian.cui, jiezhang}@utdallas.edu).

Q. Wang, V. Krishnan, and B.-M. Hodge are with the National Renewable Energy Laboratory (NREL), Golden, CO 80401, USA, e-mail: ({qin.wang, venkat.krishnan, bri.mathias.hodge}@nrel.gov).

Manuscript received, 2017.

C	Constant in an indefinite integral.
I_t	Indicator of $PICP$ in the reliability metric.
$J_{ij}^{\omega}, J_{ij}^{\mu}, J_{ij}^{\sigma}$	Elements of Jacobian matrix of the i th Gaussian model and the j th forecasting error.
$L_t^{\alpha}, U_t^{\alpha}$	Lower and upper bounds of PIs.
PDF_A	Actual PDF value of WPFEs.
$PICP$	PI coverage probability.
$PINC$	PI nominal confidence.
R_j	Residual of the j th WPFE.
$RL(\cdot)$	Ramp rule of a wind power ramp.
S_1, S_2	Objective function of the NLS method and dynamic programming in OpSDA.
S_c	Score function of the length of a time interval.
T_{fh}	Maximum forecasting horizon.
$\beta_{1-\alpha/2}$	Critical value of standard Gaussian distribution.
λ_1, λ_2	Range parameters to control the trust-region size and the correlation of random variables.
ϵ	Stopping threshold for the RNGc.
δ	Interval score rewarding the PIs.
ϕ	Tolerance value for ramp duration forecasts.
$1-\alpha$	Nominal coverage probability of PIs.
μ_i, M	Expected value of the i th Gaussian model and the set.
$\sigma_{m,n}$	Exponential covariance function of multivariate normal random number generator.
σ_i, Σ	Standard deviation of the i th Gaussian model and the set.
$\sigma_t^2, \sigma_{\hat{y}_t}^2, \sigma_{\varepsilon}^2$	Variance of the total prediction errors, model uncertainty, and noise data.
ω_i, Ω	Weight coefficient of the i th Gaussian model and the set.
$\Delta(\cdot)$	Increment of a variable as a step size.
$\Phi(\cdot)$	Standard normal distribution function.
B. Matrices and Vectors:	
Γ	Vector of overall parameter matrix of GGMM.
$\mathbf{J}^{\omega}, \mathbf{J}^{\mu},$	Jacobian matrix of ω, μ , and σ , and the overall Jacobian matrix of all parameters.
$\mathbf{J}^{\sigma}, \mathbf{J}$	Incremental matrices of ω, μ, σ , and actual probability values.
$\Delta\omega, \Delta\mu,$	Mean value and covariance matrices of the multivariate normal distribution.
$\Delta\sigma, \Delta p$	
$\mathbf{M}_{\text{MND}},$	
$\mathbf{\Sigma}_{\text{MND}}$	

I. INTRODUCTION

Large fluctuations in wind speed in a short time period can cause significant wind power ramps (WPRs) and threaten the power system's reliability [1]–[3]. WPRs can generally be divided into up-ramp, down-ramp, or non-ramp periods. This is becoming more challenging for system operators as larger wind power penetrations are seen in power systems worldwide [4].

A number of statistical and machine learning methods have been developed in the literature to forecast wind power ramps at multiple forecasting horizons. For instance, Liu *et al.* [5] developed a hybrid forecasting model to combine an orthogonal test with support vector machine. Cutler *et al.* [6] forecasted wind power ramps and evaluated the efficiency of the Wind Power Prediction Tool (WPPT) and the Mesoscale Limited Area Prediction System (MesoLAPS) for ramp forecasting. Greaves *et al.* [7] forecasted up-ramps and down-ramps with uncertain start times and incorporated a numerical weather prediction (NWP) model to reduce the forecasting errors. However, most of existing methods focus on the deterministic ramp forecasting. Probabilistic wind power ramp forecasting (p-WPRF) is expected to provide more information on forecast uncertainties, and thus produce better system schedules for balancing authorities. Among the few p-WPRF studies [8], Taylor [9] used a multinomial logit structure and categorical distribution to estimate the ramp event probabilities for different thresholds. Li *et al.* [10] provided additional probabilistic information for wind ramp occurrences by a logistic regression technique.

Both the prevalent probabilistic and statistical scenario forecasts can be used for wind power ramp forecasting. Probabilistic forecasts consider the intrinsic uncertainty in the wind power generation (or WPR) process, and give more information on the forecasted wind power and WPRs than the simple point forecasts [11]. However, they neglect the interdependence structure of forecast errors among look-ahead times, and cannot be practically used in the time-dependent and multi-stage decision-making processes, such as the design of trading strategies in a multi-market environment. Statistical scenario forecasts mainly rely on the most recent information about the interdependence structure of the prediction errors [11]. However, they should respect the probabilistic forecasts of the next time period. The intrinsic uncertainty in the wind power generation (or WPR) process and the probabilistic view of the forecasting problem are not considered in statistical scenario forecasts [11]. Pinson *et al.* [12] evaluated the quality of statistical scenario forecasts of short-term wind power generation. Ma *et al.* [13] proposed a statistical scenario forecast method considering the information of forecast error distribution and fluctuation distribution of short-term wind power generation. In this paper, we consider the advantages of both the probabilistic and statistical scenario forecasts. Probabilistic forecasts of WPR aim to provide information about the WPRF uncertainty. Statistical scenario forecasts of WPR aim to provide the time-dependent and multi-stage WPRFs that can be used in the decision-making processes.

To bridge the gap in ramp forecasting, we seek to address two critical questions for balancing authorities with the increasing WPRs integrated into power systems. Is it possible to quantitatively evaluate the probabilistic information of wind ramp occurrences, such as the ramp duration or start-time? What is the impact of different conditions on the probabilistic forecasting of WPRs, such as weather conditions (wind speed) or times of a day? This paper develops a p-WPRF method to characterize different key ramp features in different conditions. The main innovations and contributions of this paper include:

(i) developing a novel generalized Gaussian mixture model (GGMM) to fit the probability density function (PDF) of wind power forecasting errors (WPFEs); (ii) designing a statistical scenarios based p-WPRF model by using the WPFE scenarios and a novel WPR detection algorithm; and (iii) calculating and analyzing the probabilistic metrics of ramp features under different weather and time conditions.

The overall procedure of the developed p-WPRF methodology consists of four major steps. First, multiple sets of deterministic wind power forecasts are generated by a machine learning method. Second, a novel GGMM distribution model is developed to fit the actual PDF of WPFEs with a satisfactory accuracy, and the inverse transform method of GGMM is adopted to generate a large number of WPFE scenarios. Then, an optimized swinging door algorithm (OpSDA) is used to extract all the forecasting WPRs in each wind power forecasting scenario that is generated by adding the baseline wind power forecast series with a random WPFE scenario. Finally, a suite of probabilistic forecasting metrics are calculated and compared for ramping features under different conditions.

The organization of this paper is given as follows. In Section II, a WPFE scenario generation method is developed. In Section III, the methodology of p-WPRF and evaluation metrics are presented. Case studies and results analysis performed on publicly available wind power data are discussed in Section IV. Concluding remarks and future work are summarized in Section V.

II. WPFE SCENARIO GENERATION

The developed WPFE scenario generation is based on a machine learning technique to first forecast the basic wind power forecasting scenario and calculate the historical WPFEs. Then a generalized Gaussian mixture model (GGMM) is used to fit the PDF of forecasting errors. The CDF is analytically deduced. The inverse transform method based on the CDF is used to generate a large number of WPFE scenarios.

Recently, the Gaussian mixture model (GMM) has been widely used to fit the distributions of wind power generation [14], [15], load [16], and WPFEs [17], [18]. However, parameters of the GMM distribution are estimated by the expectation maximization (EM) algorithm which is strictly constrained by three constraints: (i) all the weights of mixture components must be nonnegative; (ii) the sum of all weights equals one; and (iii) the integral of each mixture component (standard normal distribution) equals one. For the developed GGMM, the non-linear least square (NLS) method is first utilized to estimate all the parameters. All the aforementioned three constraints in the GMM are not required any more in the GGMM, which means more mixture Gaussian components, even with negative weights, can be integrated in a more generalized way.

A. Analytical Expression of the GGMM PDF

The basic wind power forecasts are generated using the support vector machine (SVM) that has been widely used in the forecasting community. WPFEs are then calculated and recorded as the deviation between the basic wind power forecasts and the corresponding actual wind power. A GGMM

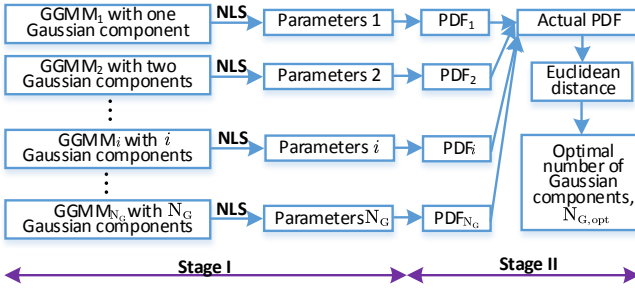


Fig. 1. Procedure of the two-stage optimization model.

distribution [14], [16], [19] is used to fit the PDF of WPFEs. The GGMM is a probabilistic model that assumes all the data points are generated from a mixture of a finite number of Gaussian distributions with multiple parameters. It is characterized by the number of mixture components, weights, mean values, and standard deviations of each component, and formulated as:

$$f(x_j|N_G; \Gamma) = \sum_{i=1}^{N_G} \omega_i g_i(x_j|\mu_i, \sigma_i), \quad \forall x_j \in \mathcal{X}, \forall i \in \mathcal{G} \quad (1)$$

where Γ defines a mixture component of the GGMM, i.e., $\Gamma = \{\omega_i, \mu_i, \sigma_i\}_{i=1}^{N_G}$. The function of each component $g(x|\mu, \sigma)$ conforms to a Gaussian function, given by:

$$g(x|\mu, \sigma) = e^{-\frac{(x-\mu)^2}{2\sigma^2}} \quad (2)$$

A two-stage optimization model is constructed to estimate all the parameters of f , i.e., N_G , ω_i , μ_i , and σ_i . In Stage I, the objective is to estimate parameters for the GGMM components using the NLS method. In Stage II, the objective is to determine the optimal number of components.

1) *Stage I*: The parameters of each GGMM are estimated by using the NLS method. For each GGMM, the number of Gaussian components is a constant, as shown in the left part of Fig. 1. The PDF of GGMM is simplified as $f(x_j|N_G; \Gamma) \xrightarrow{N_G} f(x_j|\Gamma)$. This stage aims to determine the expected value (or mean value) set M ($\mu_i \in M$), the standard deviation set Σ ($\sigma_i \in \Sigma$), and the weight coefficient set Ω ($\omega_i \in \Omega$). The NLS method using the trust-region algorithm [20] is adopted to estimate parameters (ω , μ , and σ) of mixture components of the GGMM. Given a set of data points for WPFEs (x) and their actual probabilities (p), i.e., (x_1, p_1) , ..., (x_j, p_j) , ..., (x_{N_X}, p_{N_X}) , the objective function, S_1 , of the NLS aims to minimize the sum of the squares of fitting residuals, given by:

$$S_1 = \sum_{j=1}^{N_X} R_j^2 = \sum_{j=1}^{N_X} [p_j - f(x_j|\Gamma)]^2 \quad (3)$$

Taking the mean value as an example, the minimum value of S_1 occurs when the gradient is zero, given by:

$$\frac{\partial S_1}{\partial \mu_i} = 2 \sum_{j=1}^{N_X} R_j \frac{\partial R_j}{\partial \mu_i} = -2 \sum_{j=1}^{N_X} R_j \frac{\partial f(x_j|\Gamma)}{\partial \mu_i} = 0 \quad (4)$$

Since the model contains $3 \times N_G$ parameters, there are $3 \times N_G$ gradient equations. Then, each mean value of the GGMM, μ_i , is refined iteratively by the successive approximation:

$$\mu_i \approx \mu_i^{k+1} = \mu_i^k + \Delta \mu_i \quad (5)$$

At each iteration, the GGMM is linearized by approximating to a first-order Taylor series expansion:

$$\begin{aligned} f(x_j|\Gamma) &\approx f(x_j|\Gamma^k) + \sum_{i=1}^{N_G} \frac{\partial f(x_j|\Gamma^k)}{\partial \omega_i} \Delta \omega_i \\ &+ \sum_{i=1}^{N_G} \frac{\partial f(x_j|\Gamma^k)}{\partial \mu_i} \Delta \mu_i + \sum_{i=1}^{N_G} \frac{\partial f(x_j|\Gamma^k)}{\partial \sigma_i} \Delta \sigma_i \end{aligned} \quad (6)$$

The set of the derivatives $\frac{\partial f(x_j|\Gamma^k)}{\partial \omega_i}$, $\frac{\partial f(x_j|\Gamma^k)}{\partial \mu_i}$, and $\frac{\partial f(x_j|\Gamma^k)}{\partial \sigma_i}$ constitutes the Jacobian matrix, \mathbf{J} . Each derivative is analytically deduced by:

$$J_{ij}^\omega = \frac{\partial f(x_j|\Gamma^k)}{\partial \omega_i} = e^{-\frac{(x_j - \mu_i^k)^2}{2(\sigma_i^k)^2}} \quad (7)$$

$$J_{ij}^\mu = \frac{\partial f(x_j|\Gamma^k)}{\partial \mu_i} = \frac{\omega_i^k (x_j - \mu_i^k)}{(\sigma_i^k)^2} e^{-\frac{(x_j - \mu_i^k)^2}{2(\sigma_i^k)^2}} \quad (8)$$

$$J_{ij}^\sigma = \frac{\partial f(x_j|\Gamma^k)}{\partial \sigma_i} = \frac{\omega_i^k (x_j - \mu_i^k)^2}{(\sigma_i^k)^3} e^{-\frac{(x_j - \mu_i^k)^2}{2(\sigma_i^k)^2}} \quad (9)$$

$$\mathbf{J} = [\mathbf{J}^\omega \ \mathbf{J}^\mu \ \mathbf{J}^\sigma]^T, \quad \forall J_{ij}^\omega \in \mathbf{J}^\omega, \forall J_{ij}^\mu \in \mathbf{J}^\mu, \forall J_{ij}^\sigma \in \mathbf{J}^\sigma \quad (10)$$

Since the iterative residuals are given by: $\Delta p_j = p_j - f(x_j|\Gamma^k)$, the original residuals are rearranged by:

$$\begin{aligned} R_j &= [p_j - f(x_j|\Gamma^k)] + [f(x_j|\Gamma^k) - f(x_j|\Gamma)] \\ &= \Delta p_j - \sum_{i=1}^{N_G} J_{ij}^\omega \Delta \omega_i - \sum_{i=1}^{N_G} J_{ij}^\mu \Delta \mu_i - \sum_{i=1}^{N_G} J_{ij}^\sigma \Delta \sigma_i \end{aligned} \quad (11)$$

Then substituting these expressions in (7)–(11) into the gradient equations in (4), we can rearrange and get the normal equations:

$$\sum_{j=1}^{N_X} \sum_{i=1}^{N_G} J_{ij}^\mu (J_{ij}^\omega \Delta \omega_i + J_{ij}^\mu \Delta \mu_i + J_{ij}^\sigma \Delta \sigma_i) = \sum_{j=1}^{N_X} J_{ij}^\mu \Delta p_j \quad (12)$$

$$\sum_{j=1}^{N_X} \sum_{i=1}^{N_G} J_{ij}^\omega (J_{ij}^\omega \Delta \omega_i + J_{ij}^\mu \Delta \mu_i + J_{ij}^\sigma \Delta \sigma_i) = \sum_{j=1}^{N_X} J_{ij}^\omega \Delta p_j \quad (13)$$

$$\sum_{j=1}^{N_X} \sum_{i=1}^{N_G} J_{ij}^\sigma (J_{ij}^\omega \Delta \omega_i + J_{ij}^\mu \Delta \mu_i + J_{ij}^\sigma \Delta \sigma_i) = \sum_{j=1}^{N_X} J_{ij}^\sigma \Delta p_j \quad (14)$$

The normal equations are written in the matrix notation:

$$\mathbf{J}^T \mathbf{J} \begin{bmatrix} \Delta \omega \\ \Delta \mu \\ \Delta \sigma \end{bmatrix} = \mathbf{J}^T \Delta \mathbf{p} \quad (15)$$

Since the estimated initial parameters may be far from the optimum, Equation (15) is improved by using the trust-region algorithm [20], given by:

$$[\mathbf{J}^T \mathbf{J} + \lambda_1 \text{diag}(\mathbf{J}^T \mathbf{J})] \begin{bmatrix} \Delta \omega \\ \Delta \mu \\ \Delta \sigma \end{bmatrix} = \mathbf{J}^T \Delta \mathbf{p} \quad (16)$$

where $\text{diag}(\mathbf{J}^T \mathbf{J})$ is the diagonal matrix with the same diagonal as $\mathbf{J}^T \mathbf{J}$ and λ_1 is used to control the trust-region

size. Comparing with the line search algorithm, the trust region algorithm can be used in the non-convex approximate problems (or ill-conditioned problems) due to the boundedness of the trust regions of estimated initial parameters. This advantage makes the trust region algorithm reliable and robust with strong convergence properties [21].

2) *Stage II:* After estimating the parameters of each mixture component of the GGMM, the second stage aims to determine the optimal number of mixture components, $N_{G,\text{opt}}$, by minimizing the Euclidean distance between the actual PDF, PDF_A , and the PDF of the GGMM, f , i.e., $f(x_j|N_G) \xrightarrow{N_{G,\text{opt}}} f(x_j)$, as shown in the right part of Fig. 1. The objective function is formulated as:

$$\min \sqrt{\sum_{x_j \in \mathcal{X}} [f(x_j|i) - \text{PDF}_A]^2}, \quad i = 1, 2, \dots, N_G \quad (17)$$

B. Analytical Expression of the GGMM CDF

The cumulative distribution, F , is another essential statistic metric to generate WPFE scenarios due to its monotonicity, which is analytically expressed as:

$$F(x|N_G; \boldsymbol{\Gamma}) = \int_{-\infty}^x \sum_{i=1}^{N_G} \omega_i e^{-\frac{1}{2} \left[\frac{t-\mu_i}{\sigma_i} \right]^2} dt \quad (18)$$

$$= \sum_{i=1}^{N_G} \left[\frac{\sqrt{\pi}}{2} \omega_i \sigma_i \operatorname{erf} \left(\frac{\mu_i - x}{\sigma_i} \right) \right] + C$$

$$\operatorname{erf}(x) = \frac{2}{\sqrt{\pi}} \int_0^x e^{-t^2} dt \quad (19)$$

where Equation (18) is an indefinite integral with a constant C , which can be solved by (20). Since WPFEs are normalized into the range $[0, 1]$, it can be derived that $F(x < 0) = 0$ and $F(x > 1) = 1$. Hence, we use a predefined parameter by heuristics $[h \in (-\infty, 0) \cup (1, +\infty)]$ to obtain the constant C based on the theory of the integral [22], given by:

$$C = \begin{cases} - \sum_{i=1}^{N_G} \left[\frac{\sqrt{\pi}}{2} \omega_i \sigma_i \operatorname{erf} \left(\frac{h-\mu_i}{\sigma_i} \right) \right], & h < 0 \\ 1 - \sum_{i=1}^{N_G} \left[\frac{\sqrt{\pi}}{2} \omega_i \sigma_i \operatorname{erf} \left(\frac{h-\mu_i}{\sigma_i} \right) \right], & h > 1 \end{cases} \quad (20)$$

C. Random WPFE Generation Using GGMM

To sample a random WPFE, \hat{x} , we design a random number generator (RNG) based on the GGMM (RNG-GGMM). The inverse transform method has been widely used to generate random numbers from a specific probability distribution [23], [24]. In this paper, the RNG-GGMM method utilizes the inverse function of the GGMM CDF, formulated as:

$$\hat{x} = F^{-1}[F(x|N_G; \boldsymbol{\Gamma})] \quad (22)$$

$$= F^{-1} \left\{ \sum_{i=1}^{N_G} \left[\frac{\sqrt{\pi}}{2} \omega_i \sigma_i \operatorname{erf} \left(\frac{\mu_i - x}{\sigma_i} \right) \right] + C \right\}$$

However, the inverse function in (22) cannot be analytically deduced. Alternatively, we use the Newton-Raphson method to obtain a numerical solution of the inverse CDF of the GGMM distribution. The Newton-Raphson method has been used to sample the inverse CDF of the Student's t distribution [25].

Algorithm 1: Newton-Raphson method for generating the random number of WPFEs.

```

1 Initialization: obtain a random point ( $r \in [0, 1]$ ) and
evenly partition the WPFE,  $x$ , into  $N$  regions
( $[x_n, \bar{x}_n]_{n=1}^N$ ). Decide the region where  $r$  is:
2 if  $F(\underline{x}_n) < r < F(\bar{x}_n)$  then
3   Return  $n$ ,  $x_0 = \bar{x}_n$ ; and the approximation  $x_1$  is
calculated when  $k = 0$ , by:

$$x_{k+1} = x_k - \frac{F(x_k) - r}{F'(x_k)} = x_k - \frac{F(x_k) - r}{f(x_k)}$$


$$= x_k - \frac{\sum_{i=1}^{N_G} \left[ \frac{\sqrt{\pi}}{2} \omega_i \sigma_i \operatorname{erf} \left( \frac{\mu_i - x_k}{\sigma_i} \right) \right] + C - r}{\sum_{i=1}^{N_G} \omega_i e^{-\frac{1}{2} \left[ \frac{x_k - \mu_i}{\sigma_i} \right]^2}} \quad (21)$$

4 end
5 Output the random number of one forecasting error:
6 for Iteration  $k$  from 1 to 100 do
7   if  $|x_k - x_{k-1}| < \epsilon$  then
8     | The sampled forecasting error is returned:  $\hat{x} \approx x_k$ ;
9   else
10    | The iterative process is repeated using (21).
11  end
12 end

```

The pseudocode of the forecasting error generation process is illustrated in Algorithm 1. The process repeats until the range is smaller than the stopping threshold ϵ , given by:

$$|x_k - x_{k-1}| < \epsilon \quad (23)$$

where ϵ is set as 1×10^{-8} .

A random number z is generated by the multivariate normal random number generator, and uniformed by the standard normal distribution, given by:

$$\Phi(z) = \int_{-\infty}^z \frac{1}{\sqrt{2\pi}} e^{-\frac{t^2}{2}} dt, \quad \Phi(z) \in [0, 1] \quad (24)$$

The multivariate normal random number generator mvnrnd in MATLAB is then applied to generate N_{sc} scenarios with a forecasting horizon T_{fh} using the multivariate normal distribution (MND), $z \sim N(\mathbf{M}_{MND}, \boldsymbol{\Sigma}_{MND})$. \mathbf{M}_{MND} is defined as a zero N_{sc} -by- T_{fh} matrix. $\boldsymbol{\Sigma}_{MND}$ is a T_{fh} -by- T_{fh} symmetric positive semi-definite matrix, formulated by:

$$\boldsymbol{\Sigma}_{MND} = \begin{bmatrix} \sigma_{1,1} & \sigma_{1,2} & \cdots & \sigma_{1,T_{fh}} \\ \sigma_{2,1} & \sigma_{2,2} & \cdots & \sigma_{2,T_{fh}} \\ \vdots & \vdots & \ddots & \vdots \\ \sigma_{T_{fh},1} & \sigma_{T_{fh},2} & \cdots & \sigma_{T_{fh},T_{fh}} \end{bmatrix} \quad (25)$$

where the covariance $\sigma_{m,n}$ has been modeled by an exponential covariance function in [12] and defined as:

$$\sigma_{m,n} = \text{cov}(r_m, r_n) = e^{-\frac{|m-n|}{\lambda_2}}, \quad 0 \leq m, n \leq T_{fh} \quad (26)$$

where λ_2 is used to control the strength of the correlation of random variables r_m and r_n .

The forecasting error scenarios are generated by setting a total number of N_{sc} , with a specific forecast horizon of T_{fh} (e.g., day-ahead, hours-ahead, or minutes-ahead). A large set of

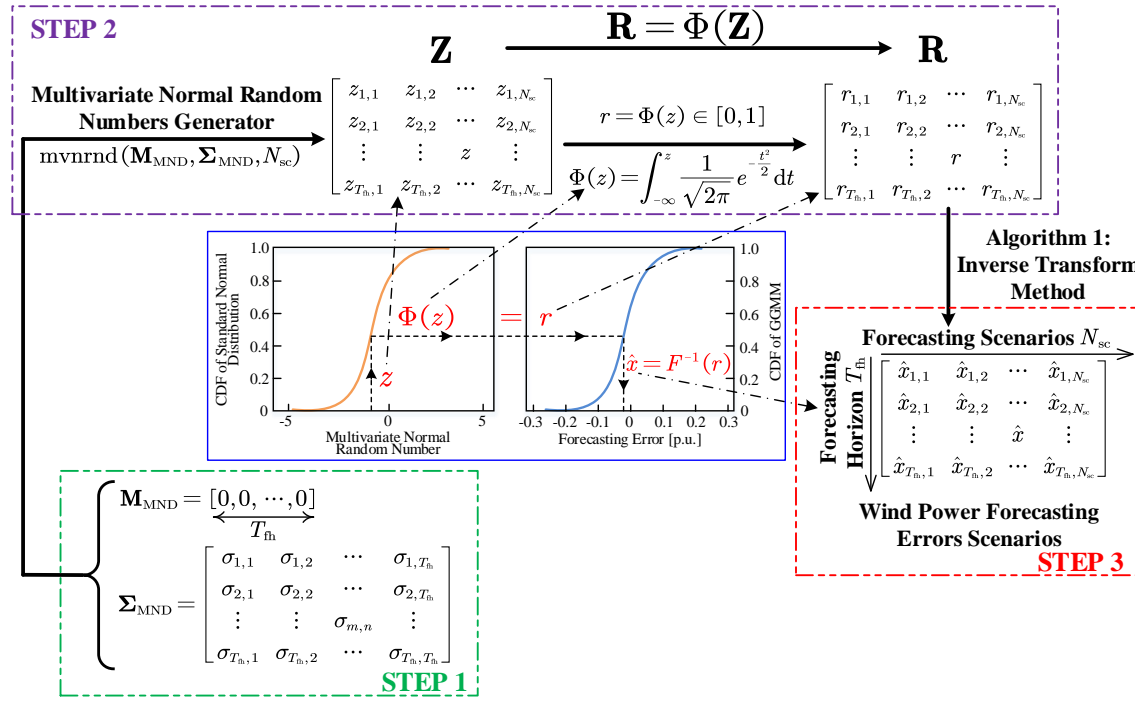


Fig. 2. The process of generating the series of WPFEs.

wind power forecasting scenarios is obtained by combining the basic deterministic wind power forecast with all the forecasting error scenarios. The schematic of the process to generate the series of WPFEs is shown in Fig. 2. This procedure is briefly described as follows:

- **Step 1:** A covariance matrix $\boldsymbol{\Sigma}_{\text{MND}}$ of the multivariate normal distribution is created. Each element $\sigma_{m,n}$ of this matrix ($\sigma_{m,n} \in \boldsymbol{\Sigma}_{\text{MND}}$) is calculated by (26).
- **Step 2:** The random number matrix \mathbf{Z} is directly created by the multivariate normal random numbers generator `mvnrnd` built in MATLAB [26], i.e., $\mathbf{Z} \sim \text{mvnrnd}(\mathbf{M}_{\text{MND}}, \boldsymbol{\Sigma}_{\text{MND}}, N_{\text{sc}})$. The matrix \mathbf{Z} is a N_{sc} -by- T_{fh} matrix of random numbers. Each element z of \mathbf{Z} ($z \in \mathbf{Z}$) is transformed into the uniform distribution by the standard normal distribution $\Phi(z)$ in (24). Then, the uniform random number r is generated as: $r = \Phi(z)$. Correspondingly, the uniform random number matrix \mathbf{R} is also generated as: $\mathbf{R} = \Phi(\mathbf{Z})$.
- **Step 3:** Each element r of the uniform random number matrix \mathbf{R} is transformed into the forecast error, as shown in the right part of Fig. 2. The corresponding WPFE \hat{x} is estimated by the inverse transform method of the GGMM using Algorithm 1, i.e., $\hat{x} = F^{-1}(r)$. After all uniform random numbers are transformed to WPFEs, the series of WPFEs is generated with respect to both the forecasting horizon T_{fh} and forecasting scenarios N_{sc} simultaneously.

III. P-WPRF METHODOLOGY AND EVALUATION METRICS

A. Wind Power Ramps Detection

Based on the generated wind power forecasting scenarios, an OpSDA method [27] is used to detect all the WPRs at each timescale. In the OpSDA, the conventional swinging door algorithm (SDA) with a predefined value is first applied to

segregate the wind power data into multiple discrete segments. Then dynamic programming is used to merge adjacent segments with the same ramp direction and relatively high ramp rates. A brief description of the OpSDA is introduced here, and more details can be found in [27]. Subintervals that satisfy the ramp rules are rewarded by a score function; otherwise, their score is set to zero. The current subinterval is retested as above after being combined with the next subinterval. This process is performed recursively until the end of the dataset. A positive score function, S_c , is designed based on the length of the interval segregated by the SDA. Given a time interval (m, n) in the forecasting horizon and an objective function, S_2 , of the dynamic programming, a WPR is detected by maximizing the objective function, S_2 :

$$S_2(m, n) = \max_{m < v < n} [S_c(m, v) + S_2(v, n)], \quad m < n \quad (27)$$

s.t.

$$S_c(m, n) > S_c(m, v) + S_c(v + 1, n), \quad \forall m < v < n \quad (28)$$

$$S_c(m, n) = (m - n)^2 \times RL(m, n), \quad \forall m < v < n \quad (29)$$

where the positive score function, S_c , conforms to a superadditivity property in (28) and is formulated in (29). The ramp rule, $RL(m, n)$, is defined as the change in wind power magnitude without ramp duration limits [28], [29]. Thus, the WPR is defined as the wind power change that exceeds the threshold (15% of the installed wind capacity) without constraining the ramping duration. A brief example of WPRs detection in one day is illustrated in Fig. 3. It is shown in Fig. 3a that the conventional SDA only detects one WPR without any optimization. As shown in Fig. 3b, the OpSDA is able to combine the adjacent segments in the same direction and detect WPRs more accurately.

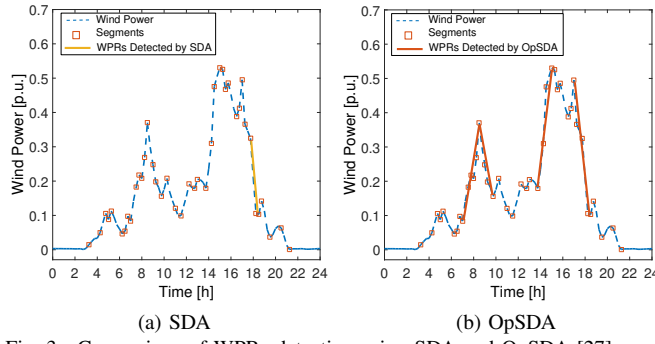


Fig. 3. Comparison of WPRs detection using SDA and OpSDA [27].

B. PI-Based WPRF Metrics

To evaluate the performance of p-WPRF, two predictive intervals (PIs) based metrics, namely reliability and sharpness [30]–[32], are briefly introduced in this section. Reliability is the correct degree of a p-WPRF assessed by the hit percentage. Sharpness is the uncertainty conveyed by the p-WPRF.

1) Reliability: Based on the set of WPRFs, a $100(1-\alpha)\%$ confidence level PI of the measured WPRs can be expressed with the lower bound L_t^α and the upper bound U_t^α as the PI nominal confidence (PINC), given by:

$$L_t^\alpha = \hat{y}_t + \hat{x}_t^s - \beta_{1-\alpha/2}\sigma_t \quad (30)$$

$$U_t^\alpha = \hat{y}_t + \hat{x}_t^s + \beta_{1-\alpha/2}\sigma_t \quad (31)$$

$$\sigma_t^2 = \sigma_{\hat{y}_t}^2 + \sigma_\varepsilon^2 \quad (32)$$

$$\sigma_{\hat{y}_t} = \sqrt{\frac{1}{N_{sc}} \sum_{s=1}^{N_{sc}} \left[\hat{y}_t + \hat{x}_t^s - \frac{1}{N_{sc}} \sum_{s=1}^{N_{sc}} (\hat{y}_t + \hat{x}_t^s) \right]^2} \quad (33)$$

where σ_t^2 , $\sigma_{\hat{y}_t}^2$, and σ_ε^2 represent the variance of the total prediction errors, model uncertainty, and noise data, respectively. σ_t^2 can be calculated by using (32) [30]. $\sigma_{\hat{y}_t}^2$ can be calculated by using (33). The noise date can be calculated by the measured and forecasting data, i.e., $\varepsilon = y - (\hat{y} + \hat{x})$.

The future measured wind power ramps are expected to lie within the PI bounds with a prescribed probability termed as the nominal proportion. It is expected that the coverage probability of obtained PIs will asymptotically reach the nominal level of confidence (ideal case) over the full WPRs. PI coverage probability (PICP) is a critical measure for the reliability of the WPR PIs, formulated in (34), where the indicator of PICP, I_t , is defined in (35).

$$PICP = \frac{1}{N_W} \sum_{t=1}^{N_W} I_t \times 100\% \quad (34)$$

$$I_t = \begin{cases} 1, & y_t \in [L_t^\alpha, U_t^\alpha] \\ 0, & y_t \notin [L_t^\alpha, U_t^\alpha] \end{cases} \quad (35)$$

Theoretically, the PICP should be close to the corresponding PINC. The average coverage error (ACE) [30] metric should be as close to zero as possible. A smaller absolute ACE indicates more reliable PIs of WPRs.

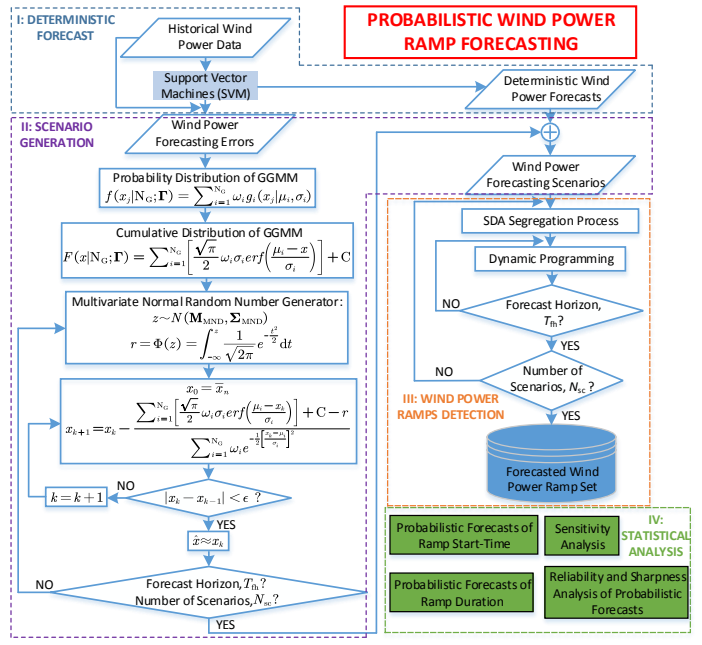


Fig. 4. The overall framework for developing the p-WPRF.

2) Sharpness: Sharpness is calculated as the average interval size of different confident levels. A measure of sharpness, δ , is given by the mean size of PIs, formulated in (36). The interval score δ rewards the narrow PI and gives penalty if the target does not lie within the estimated PI.

$$\delta = \frac{1}{N_{RF}} \sum_{i=1}^{N_{RF}} \left[\frac{1}{N_W} \sum_{t=1}^{N_W} (U_t^\alpha - L_t^\alpha) \right] \times 100\% \quad (36)$$

where N_{RF} is the total number of ramping features, including up- and down-ramp duration, up- and down-ramp magnitude, up- and down-ramp rate, and up- and down-ramp start-time.

The average interval score (AIS) can be employed to comprehensively evaluate the overall skill of WPR PIs to assess the sharpness. Generally, smaller ACE, δ , and AIS indicate a better forecasting performance of p-WPRF.

C. Procedure of p-WPRF

The p-WPRF methodology is developed by using a large number of forecast scenarios, and extracting corresponding ramps using the OpSDA method described before. The overall framework for generating p-WPRF is illustrated in Fig. 4, which consists of four major steps: deterministic wind power forecasting, forecasting scenario generation, wind power ramp detection, and probabilistic ramp forecasting and analysis. The four major steps are described as follows:

- Step 1:** Based on historical wind power data, a machine learning method, (i.e., SVM), is used to generate deterministic wind power forecasts.
- Step 2:** Historical WPFEs are generated from the basic forecasting model, as described in Section II. The GGMM distribution model is adopted to fit the probability distribution of historical WPFEs and the cumulative distribution of GGMM is analytically deduced. The inverse transform method is used to simulate a large number of WPFE scenarios, as described in Section II-C.

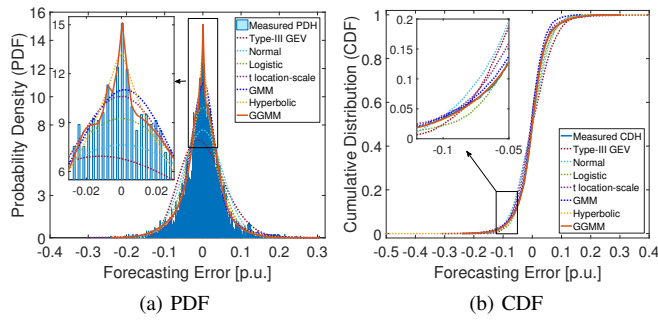


Fig. 5. Probability and cumulative distributions of WPFEs using seven distribution models. Generalized Extreme Value: $\mu = -0.0214, \sigma = 0.0537, \kappa = -0.1597$; Normal: $\mu = 1.72 \times 10^{-6}, \sigma = 0.0522$; Logistic: $\mu = -3.09 \times 10^{-4}, \sigma = 0.027$; t Location-Scale Distribution: $\mu = -2.53 \times 10^{-4}, \sigma = 0.0346, \nu = 3.11$; and Hyperbolic: $\pi = 4.72 \times 10^{-3}, \zeta = 2.09 \times 10^{-4}, \delta = 7.69 \times 10^{-6}, \mu = -3.39 \times 10^{-4}$.

- **Step 3:** A wind power forecasting scenario is generated by adding the basic forecasting data with each individual WPFE scenario. Each scenario is put into the OpSDA algorithm to extract all the significant WPRs.
- **Step 4:** The p-WPRF is generated and analyzed by using a set of probabilistic forecasting metrics, as described in Section III-B.

IV. CASE STUDIES AND RESULTS

A. Test Case

The developed data-driven WPRF model is verified using the Wind Integration National Dataset (WIND) Toolkit [33]. The data represents wind power generation from January 1st 2007 to December 31st 2012. The wind plants used in this analysis are from 711 wind sites near Dallas, Texas, with a 5-minute data resolution. The total rated wind power capacity is 9,987 MW. All case studies are carried out using the MATLAB 2016a on two Intel-e5-2603 1.6-GHz workstations with 32 GB of RAM memory. The door width of the OpSDA is set as 0.2% of the rated capacity.

B. Performance of Different Distribution Models for WPFEs

Fig. 5 compares the probability and cumulative distributions of WPFEs from seven distributions (i.e., Generalized Extreme Value (GEV), Normal, Logistic, t Location-Scale, GMM, Hyperbolic, and GGMM distributions). The probability density histogram (PDH) and cumulative distribution histogram (CDH) of the measured WPFEs are used as the benchmark to estimate the parameters of the distribution models. The parameters of GEV, Normal, Logistic, t Location-Scale, and Hyperbolic distributions are estimated from the sampled WPFEs by using the maximum likelihood estimation (MLE), which can be implemented by the fitting function `fitdist` built into the Statistics Toolbox in MATLAB [34]. Parameters of the GMM distribution are estimated by the fitting function `fitgmdist` built into the Statistics Toolbox in MATLAB [35] using the EM algorithm. Estimated parameters of the GMM and the developed GGMM are listed in Table I. The coefficient of determination, R^2 , is used to evaluate the correlation between the observed and modeled data values. The GEV distribution has the smallest coefficient of determination, 0.9041, and the GGMM distribution shows the largest coefficient of determination, 0.9922. The coefficients of determination of Normal,

TABLE I
ESTIMATED PARAMETERS OF GMM AND THE DEVELOPED GGMM

Components No.	Weight (ω)		Mean (μ)		Standard Dev. (σ)	
	GMM	GGMM	GMM	GGMM	GMM	GGMM
Comp. 1	0.3893	-0.4208	-0.0112	-0.0030	0.0044	0.0040
Comp. 2	0.5808	0.4211	0.0015	-0.0030	0.0007	0.0040
Comp. 3	0.0299	0.9098	0.1159	-0.0205	0.0044	0.0065
Comp. 4	/	0.5873	/	0.0034	/	0.0404
Comp. 5	/	0.2076	/	-0.0089	/	0.0944

TABLE II
COMPARISON OF THE ACE RELIABILITY METRIC USING DIFFERENT p-WPRF MODELS UNDER DIFFERENT WEATHER CONDITIONS [UNIT: %]

p-WPRF models	Wind speed			
	Light	Gentle	Strong	Gale
QFWP scenarios	18.83	21.76	24.92	19.49
WPFE scenarios w/o calibration	9.43	12.56	15.56	10.28
WPFE scenarios with calibration	2.37	4.81	7.49	2.57

Logistic, t Location-Scale, GMM, and Hyperbolic distributions are 0.9352, 0.9698, 0.9828, 0.9855, and 0.9873, respectively. Both the coefficient of determination and Fig. 5 show that the GGMM distribution outperforms other distributions in modeling WPFEs.

Note that the GEV distribution is often used to model the smallest or largest value among a large set of independent and identically distributed random values (representing measurements or observations). The GEV combines three simpler distributions into a single form, allowing a continuous range of possible shapes that includes simpler distributions [36]. The mathematical formulation of the PDF for the GEV distribution can be expressed as:

$$f(x|\mu, \sigma, \kappa) = \frac{1}{\sigma} \exp\left(-\left(1+\kappa \frac{(x-\mu)}{\sigma}\right)^{-\frac{1}{\kappa}}\right) \left(1+\kappa \frac{(x-\mu)}{\sigma}\right)^{-1-\frac{1}{\kappa}} \quad (37)$$

where μ is the location parameter and estimated as -0.0214. σ is the scale parameter and estimated as 0.0537. κ is the shape parameter and estimated as -0.1597. Theoretically, if $\kappa=0$, GEV is referred to as Type I (Gumbel); if $\kappa>0$, GEV is referred to as Type II (Frechet); and if $\kappa<0$, GEV is referred to as Type III (Weibull). Thus, the Type-III GEV is used for comparison in this case.

C. p-WPRF Results Under Different Weather Conditions

Weather conditions (wind speed) are divided into multiple categories according to different wind speeds. In this case study, four wind speed categories are considered: light wind speed (0-11 km/h), gentle wind speed (12-29 km/h), strong wind speed (30-50 km/h), and gale wind speed (≥ 51 km/h) [37]. To calibrate the p-WPRF results, the distribution of WPFEs is modeled under different conditions by dividing the wind power into multiple power bins. The conditional distribution of WPFEs is then modeled for each power bin and used to calibrate the p-WPRF results. Detailed information about the conditional distribution of WPFEs can be seen in [38].

Fig. 6 compares the PICP curves under different wind speed conditions using different p-WPRF models with calibration.

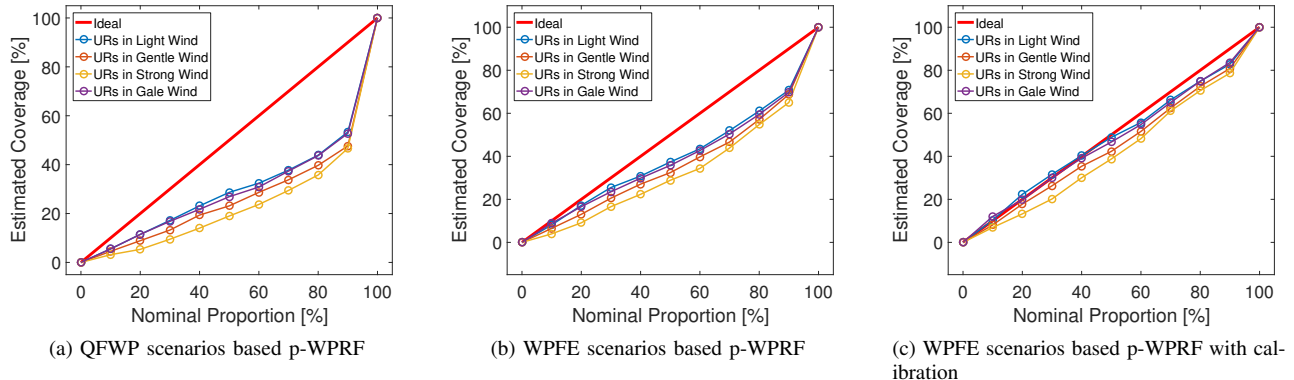


Fig. 6. Comparison of reliability metrics under different weather conditions based on p-WPRF models and calibration: (a) quantile forecast of wind power (QFWP) scenarios based p-WPRF (developed in [10]); (b) WPFE scenarios based p-WPRF (developed in this paper); and (c) WPFE scenarios based p-WPRF with calibration.

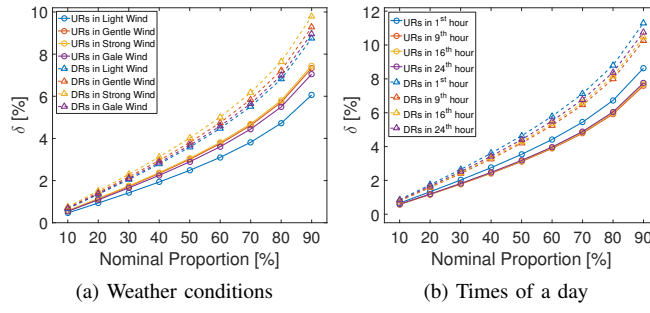


Fig. 7. Comparison of sharpness metrics for both upward ramps (URs) and downward ramps (DRs): (a) weather conditions and (b) times of a day.

Table II compares the ACE reliability metric using different p-WPRF models with the calibration. The quantile forecast of wind power (QFWP) scenarios based p-WPRF model developed in [10] is adopted as the benchmark, as shown in Fig. 6a. Fig. 6b shows the PICP curves from the WPFE scenarios based p-WPRF model (developed in this paper), which are closer to the PINC curve than those using the QFWP scenarios based p-WPRF. Fig. 6c shows the PICP curves using the WPFE scenarios based p-WPRF with calibration, which are closer to the PINC curve than those without calibration in Fig. 6b. Both Fig. 6 and Table II show the superiority of the proposed p-WPRF model, and also verify the effectiveness of the calibration process.

As shown in Fig. 6, the light wind speed condition shows the best reliability with the blue solid line closest to the ideal case (red line). The strong wind speed condition shows the worst reliability with the yellow solid line farthest from the ideal case (red line). As shown in Fig. 7a, the light wind speed condition shows the narrowest PIs represented by the smallest interval score (δ), and the strong wind speed condition shows the widest PIs represented by the largest interval score (δ). This finding corresponds to the uncertainties in WPFEs as shown in Fig. 9a, which are represented by the standard deviation σ . The light wind speed condition shows the lowest uncertainty with the smallest standard deviation ($\sigma_{\text{Light}}=20.87$ MW). The strong wind speed condition shows the highest uncertainty with the largest standard deviation ($\sigma_{\text{Strong}}=58.43$ MW). This phenomenon can be explained by the nonlinearity of the wind turbine power curve [39]. For the light, gentle, and gale wind conditions, the wind power generation varies

TABLE III
COMPARISON OF THE ACE RELIABILITY METRIC USING DIFFERENT P-WPRF MODELS AT DIFFERENT TIMES OF DAY [UNIT: %]

p-WPRF models	Times of a day			
	1 st hour	9 th hour	16 th hour	24 th hour
QFWP scenarios	19.15	17.91	18.43	19.89
WPFE scenarios w/o calibration	7.53	6.34	6.05	8.11
WPFE scenarios with calibration	4.94	3.79	3.67	5.96

within a relatively smaller range. However, for the strong wind condition, the wind power generation varies within a large range, and a small change in wind speed will cause a large change in wind power generation. The varying large range of the wind power generation will correspondingly increase the distributed range of WPFEs, which presents a heavy tail and low peak distribution of WPFEs under the strong wind condition (as shown in Fig. 9a). This phenomenon shows that the WPRFs under the strong wind condition are critically important for power system operations, and more challenging compared to other wind conditions.

D. p-WPRF Results at Different Times of a Day

The p-WPRF is also affected by the time of a day. For a better illustration, four representative time periods are chosen: 1st, 9th, 16th, and 24th hours. The same calibration method in Section IV-C is used to improve the p-WPRF results. Fig. 8 compares the PICP curves at different times of the day using different p-WPRF models with calibration. Table III compares the ACE reliability metric using different p-WPRF models with calibration. The case using the QFWP scenarios-based p-WPRF in [10] is taken as the benchmark, as shown in Fig. 8a. The PICP curves using the WPFE scenarios-based p-WPRF in Fig. 8b are closer to the PINC curve than those using the QFWP scenarios-based p-WPRF model. The PICP curves using the WPFE scenarios-based p-WPRF with calibration in Fig. 8c are closer to the PINC curve than those without calibration.

As shown in Fig. 8, the p-WPRFs at the 9th hour and the 16th hour show the best reliability performance and are represented by the orange and yellow solid lines, respectively, that are closest to the ideal case (red line), though the results are fairly similar over all of the hours. The p-WPRFs at the 1st hour and

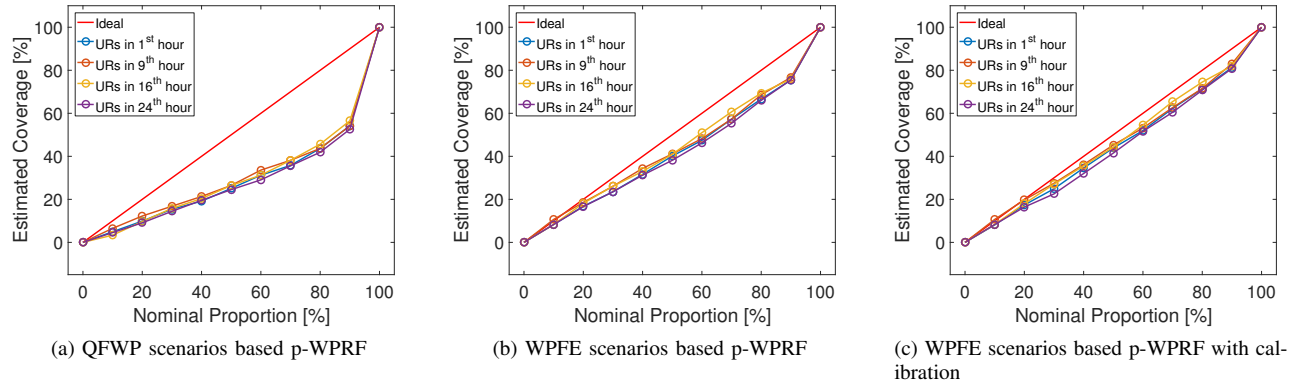


Fig. 8. Comparison of reliability metrics at different times of a day based on p-WPRF models and calibration: (a) QFWP scenarios based p-WPRF (developed in [10]); (b) WPFE scenarios based p-WPRF (developed in this paper); and (c) WPFE scenarios based p-WPRF with calibration.

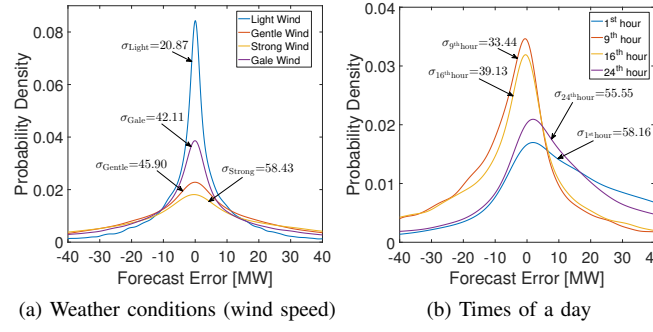


Fig. 9. WPFE distributions under different weather conditions and times of a day.

the 24th hour show the worst reliability metric represented by the blue and purple solid lines, respectively. As shown in Fig. 7b, the p-WPRF at the 9th hour shows the narrowest PIs with the smallest interval score (δ), and the p-WPRF at the 1st hour shows the widest PIs with the largest interval score (δ). This finding is consistent with the uncertainties of WPFEs, which are represented by the standard deviation σ as seen in Fig. 9b. This finding is also correlated with that under different weather conditions in Section IV-C. For this case, the results at the 1st hour and 24th hour have stronger relationship with those under the strong wind condition due to similar uncertainties ($\sigma_{\text{Strong}}=58.43$, $\sigma_{1^{\text{st}}\text{hour}}=58.16$, and $\sigma_{24^{\text{th}}\text{hour}}=55.55$). This is because the wind speed is generally stronger at night. This correlation between the weather condition and the time of the day can be further explored and possibly considered in the conditional ramp forecasting model.

In Section IV-C, the standard deviations of WPFEs under the light, gentle, strong, and gale wind speed conditions are 20.87 MW, 45.90 MW, 58.43 MW, and 42.11 MW, respectively. The AISs under the light, gentle, strong, and gale wind speed conditions are 3.38%, 3.79%, 3.94%, and 3.66%, respectively. In Section IV-D, the standard deviations of WPFEs for the 1st, 9th, 16th, and 24th hours are 58.16 MW, 33.44 MW, 39.13 MW, and 55.55 MW, respectively. The AISs for the 1st, 9th, 16th, and 24th hours are 4.55%, 4.07%, 4.14%, and 4.23%, respectively. According to the empirical criteria of correlation in [40], the correlation coefficients between standard deviations of WPFEs and AISs are 0.9905 and 0.8319 for both cases in Section IV-C and IV-D, respectively. It indicates that there exists a *high correlation* (0.8~1.0) between the standard deviation of WPFEs and the performance of the p-WPRF model.

TABLE IV
CORRELATION BETWEEN UNCERTAINTIES OF p-WPRF AND RELIABILITY & SHARPNESS METRICS UNDER DIFFERENT WEATHER CONDITIONS

Uncertainties of WPRF [%]	Up-Ramps		Down-Ramps	
	ACE [%]	AIS [%]	ACE [%]	AIS [%]
4.01	37.17	3.41	29.85	4.47
3.17	30.83	3.35	17.44	4.24
2.71	21.71	3.22	14.99	4.09
1.72	18.67	2.77	13.29	3.99

TABLE V
CORRELATION BETWEEN UNCERTAINTIES OF p-WPRF AND RELIABILITY & SHARPNESS METRICS AT DIFFERENT TIMES OF A DAY

Uncertainties of WPRF [%]	Up-Ramps		Down-Ramps	
	ACE [%]	AIS [%]	ACE [%]	AIS [%]
6.25	30.11	3.94	26.58	5.16
5.41	28.84	3.54	23.63	4.91
4.84	23.84	3.51	16.43	4.78
2.44	22.43	3.47	13.95	4.68

relation (0.8~1.0) between the standard deviation of WPFEs and the performance of the p-WPRF model.

E. Uncertainty Analysis of WPRF in Different Conditions

For a better illustration, the uncertainties of p-WPRF in both Section IV-C and Section IV-D are sorted in descending order for analysis. Table IV and Table V show the correlation between uncertainties of p-WPRF and the performance metrics in Section IV-C and Section IV-D, respectively. ACE and AIS represent reliability and sharpness metrics, respectively. The uncertainties of WPRF are represented by the standard deviation of forecasted WPRs. The p-WPRF performs better with smaller ACE and AIS values due to the decrease of uncertainties of p-WPRF. In Table IV, the 2.29% decrease of uncertainties of p-WPRF can reduce ACE by 18.51% and 16.56% for up- and down-ramps, respectively. It can also reduce AIS by 0.64% and 0.48% for up- and down-ramps, respectively. In Table V, the 3.81% decrease of uncertainties of p-WPRF can reduce ACE by 7.68% and 12.63% for up- and down-ramps, respectively. It can also reduce AIS by 0.47% and 0.48% for up- and down-ramps, respectively.

F. Delivered Output and Analysis of the Developed p-WPRF

1) *Ramp Duration Probabilistic Forecasts:* Based on the wind power forecasting scenarios, the number of WPRs occurring within a tolerance value, ϕ , is calculated and expressed

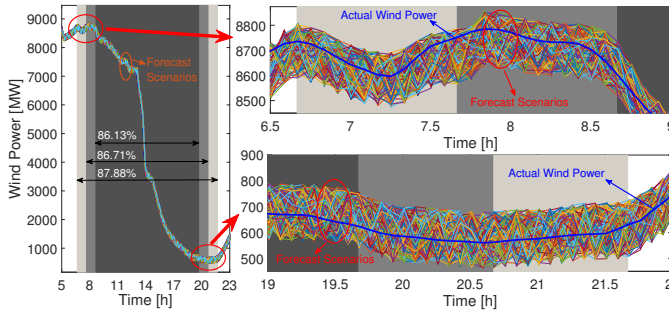


Fig. 10. Probabilistic ramp duration forecasts illustrated with banded areas.

TABLE VI
PROBABILISTIC FORECASTING RESULTS OF RAMP DURATION

Ramp Duration		Probability [%]
Start-Time	End-Time	
13:25	14:55	43.93
13:20	15:00	77.46
13:15	15:05	91.91
13:10	15:10	96.53

by N_ϕ . The forecasting probability of the WPRs within the tolerance value, ϕ , are formulated as $\Pr(N_\phi, N_{sc} | \phi) = N_\phi / N_{sc}$. The probability of ramp duration for one WPR is illustrated in Fig. 10. Three cases with different ramp duration tolerance values are studied: without tolerance ($\phi=0$), 5-minute tolerance ($\phi=1$), 10-minute tolerance ($\phi=2$), 15-minute tolerance ($\phi=3$), and 20-minute tolerance ($\phi=4$). For each WPR, the occurrence probability is calculated within a certain time interval. The probability of WPR occurrence is increased with increasing the tolerance value, as illustrated by the wider banded areas. The sensitivity of ramp duration probability to the tolerance value is analyzed in Fig. 11. It is shown that the probability of wind power ramp duration also increases with increasing the tolerance value for both upward and downward ramps. This information could be potentially used by power system operators to approximately estimate the probability of WPRs according to the corresponding tolerance value. For instance, if the power system operators set a 5-minute tolerance value ($\phi=1$), the probability of correctly forecasting a ramp is larger than 60% for all ramps.

The probabilistic forecasting results of ramp duration with an hour and a half period are shown in Table VI. As can be seen, the probability of ramp duration lasting from 13:25 to 14:55 is 43.93%; the probability of ramp duration lasting from 13:20 to 15:00 is 77.46%; the probability of ramp duration lasting from 13:15 to 15:05 is 91.91%; and the probability of ramp duration lasting from 13:10 to 15:10 is 96.53%.

2) *Ramp Start-Time Probabilistic Forecasts:* In addition to the occurrence probability of ramp duration, balancing authorities are also concerned with the probability of ramp start-time in order to prepare sufficient ancillary services, such as ramp reserves [41]. Fig. 12 illustrates the probability of up- and down-ramp start-time. For up-ramps in Fig. 12a, the 1st, 3rd, and 5th up-ramps start with a probability higher than 50%, namely 58.05% (65th minute), 61.49% (355th minute), and 98.17% (480th minute), respectively. For down-ramps in Fig. 12b, the 4th, 5th, and 6th down-ramps start with a probability higher than 80%, namely 90.81% (330th minute), 85.63% (400th minute), and 98.85% (475th minute), respectively.

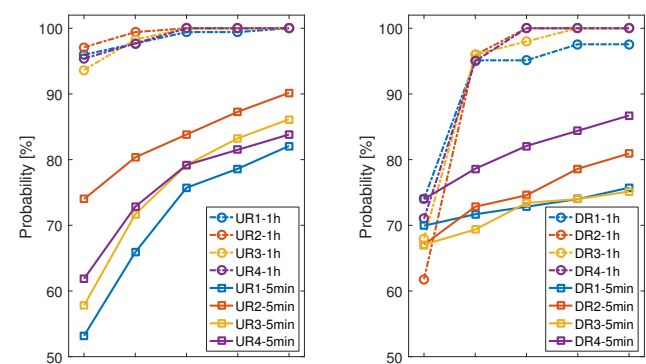


Fig. 11. Sensitivity of wind ramp duration probability to the tolerance value at the 5-minute and 1-hour timescale forecasts.

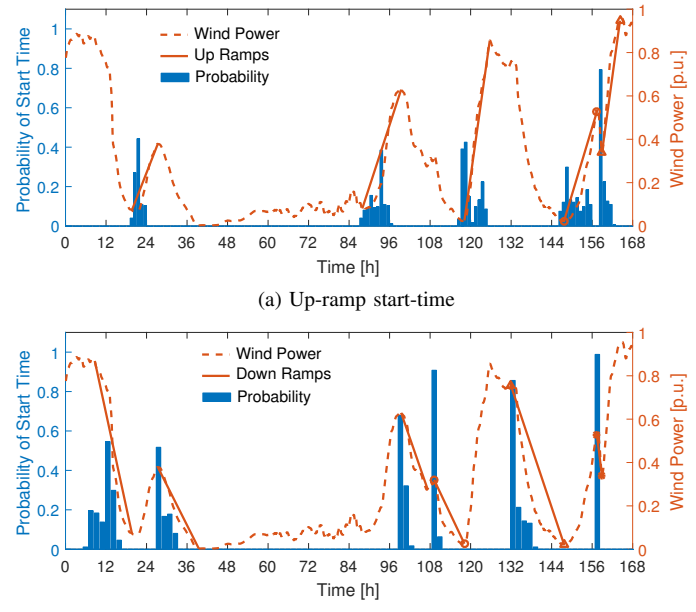


Fig. 12. Probabilistic forecasts of up- and down-ramp start-time.

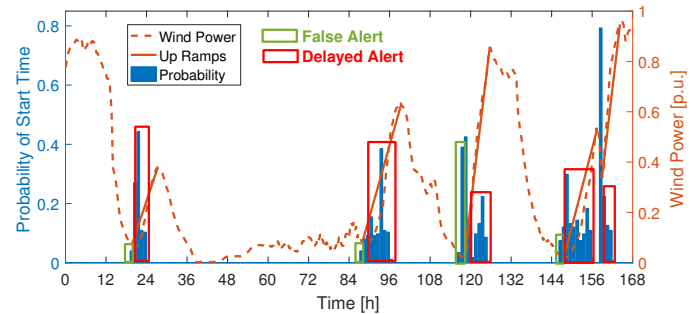


Fig. 13. Probabilistic forecasts of start-time considering false and delayed alerts.

3) *Ramp Rate Probabilistic Forecasts:* The developed p-WPRF model can also provide probabilistic forecasting information for balancing authorities, which can be used to design probabilistic wind power ramping products [42]. Table VII shows the probabilistic forecasting results of ramp rate using the developed p-WPRF model, where both ramp rate values and the corresponding maximum probability are enumerated. As can be seen, the first ramp (Ramp #1) presents the highest

TABLE VII
PROBABILISTIC FORECASTING RESULTS OF RAMP RATE

Ramp No.	Ramp Rate [MW/h]	Prob. [%]	Ramp No.	Ramp Rate [MW/h]	Prob. [%]
Ramp #1	550	87.35	Ramp #4	620	81.03
Ramp #2	600	66.67	Ramp #5	1,300	75.86
Ramp #3	750	62.64	Ramp #6	1,050	74.71

TABLE VIII
PROBABILITIES OF FALSE AND DELAYED ALERTS OF WPRFs

Number of Ramps	Actual Time	False Alerts		Delayed Alerts	
		Time [h]	Prob. [%]	Time [h]	Prob. [%]
Ramp #1	20	19	4.31	21	48.67
		-	-	22	1.03
		-	-	23	9.54
Ramp #2	89	88	4.19	90	18.22
		-	-	91	15.46
		-	-	92	39.45
Ramp #3	118	116	4.43	120	11.32
		117	38.12	121	14.69
		-	-	122	21.63
Ramp #4	147	146	9.12	148	37.48
		-	-	149	12.43
		-	-	150	11.55
Ramp #5	158	-	-	159	19.35
		-	-	160	15.89
		-	-	161	14.77

probability value (87.35%) with the ramp rate of 550 MW/h. The third ramp (Ramp #3) shows the lowest probability value (62.64%) with the ramp rate of 750 MW/h. The occurrence probabilities of the other four ramps (i.e., 600 MW/h for Ramp #2, 620 MW/h for Ramp #4, 1,300 MW/h for Ramp #5, and 1,050 MW/h for Ramp #6) are 66.67%, 81.03%, 75.86%, and 74.71%, respectively. These numerical results (the maximum probability and ramp rate values) can be utilized in the stochastic unit commitment problem to help reduce the unexpected costs caused by WPRs.

4) *False and Delayed Alerts of WPRFs:* False alerts of WPRFs are provided before the actual ramp event occurs. Delayed alerts of WPRFs are provided after the actual ramp event occurs. Based on the results in Fig. 12a, Fig. 13 shows the probabilistic forecasts of start-time considering the false and delayed alerts with a lower tolerance. Table VIII shows the probabilities of false and delayed alerts at different times. The forecasts of four ramps show different levels of false alerts. For the third ramp, the actual start-time is at the 118th hour. A false alert occurs at the 117th hour with an occurrence probability of 38.12%, and at the 116th hour with an occurrence probability of 4.43%. For the first, second, and fourth ramps, the false alerts occur with relatively smaller occurrence probabilities of 4.31%, 4.19%, and 9.12%, respectively. Thus, more attention should be paid to the third ramp considering the false alert with a high probability, which may cause unnecessary operations and control strategies. In addition, delayed alerts may have higher impacts on the reliability and economics benefits of power systems than false alerts. Under this circumstance, conventional generators cannot be committed when needed for ramping due to delayed alerts of WPRFs.

V. CONCLUSION

This paper developed a data-driven probabilistic wind power ramp forecasting (p-WPRF) method based on a large number of wind power forecasting scenarios. A deterministic wind power forecast was first generated by a machine learning method, and then used to calculate historical forecasting errors. A continuous generalized Gaussian mixture model (GGMM) was utilized to fit the probability distribution function (PDF) of wind power forecasting errors (WPFEs) and to analytically deduce the corresponding cumulative distribution function (CDF). The inverse transform method based on the CDF was used to generate a large number of WPFE scenarios. An optimized swinging door algorithm (OpSDA) was used to extract all the WPRs for the statistical analysis of p-WPRFs. Numerical simulations on publicly available wind power data showed some universal and common lessons as follows:

- (i) The GGMM distribution outperformed other distributions, including the widely used GMM distribution, in modeling the probability distribution of WPFEs.
- (ii) There exists a *high correlation* between the standard deviation of WPFEs and the performance of the p-WPRF model. The reduction of WPFEs could significantly enhance the performance of the p-WPRF model.
- (iii) The probability of wind power ramp duration increased with the increasing ramp duration tolerance value for both upward and downward ramps.

In the future, this research can be further improved by: (i) developing probabilistic wind power ramp products in the electricity market design; and (ii) studying the p-WPRF method in multiple timescales. To improve the robustness of the proposed WPRF methodology under extreme weather conditions (especially for the strong wind condition), this work can be further extended by: (i) improving the robustness of wind power probabilistic forecasts and the forecasting accuracy of Numerical Weather Prediction models; and (ii) considering the uncertainty of space-time dependencies of various nearby locations and look-ahead times.

ACKNOWLEDGMENT

This work was supported by the National Renewable Energy Laboratory under Subcontract No. XHQ-6-62546-01 (under the U.S. Department of Energy Prime Contract No. DE-AC36-08GO28308). The authors would also like to thank the five anonymous reviewers for their constructive suggestions to this research.

REFERENCES

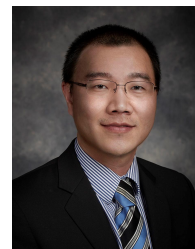
- [1] Y. Qi and Y. Liu, "Wind power ramping control using competitive game," *IEEE Trans. Sustain. Energy*, vol. 7, no. 4, pp. 1516–1524, Oct. 2016.
- [2] M. Cui, D. Ke, Y. Sun, D. Gan, J. Zhang, and B.-M. Hodge, "Wind power ramp event forecasting using a stochastic scenario generation method," *IEEE Trans. Sustain. Energy*, vol. 6, no. 2, pp. 422–433, Apr. 2015.
- [3] H. Jiang, Y. Zhang, J. J. Zhang, D. W. Gao, and E. Muljadi, "Synchrophasor-based auxiliary controller to enhance the voltage stability of a distribution system with high renewable energy penetration," *IEEE Trans. Smart Grid*, vol. 6, no. 4, pp. 2107–2115, Jul. 2015.
- [4] Q. Xu, N. Zhang, C. Kang, Q. Xia, D. He, C. Liu, Y. Huang, L. Cheng, and J. Bai, "A game theoretical pricing mechanism for multi-area spinning reserve trading considering wind power uncertainty," *IEEE Trans. Power Syst.*, vol. 31, no. 2, pp. 1084–1095, Mar. 2016.

- [5] Y. Liu, Y. Sun, D. Infield, Y. Zhao, S. Han, and J. Yan, "A hybrid forecasting method for wind power ramp based on Orthogonal Test and Support Vector Machine (OT-SVM)," *IEEE Trans. Sustain. Energy*, vol. 8, no. 2, pp. 451–457, Apr. 2017.
- [6] N. Cutler, M. Kay, K. Jacka, and T. S. Nielsen, "Detecting categorizing and forecasting large ramps in wind farm power output using meteorological observations and WPPT," *Wind Energy*, vol. 10, no. 5, pp. 453–470, Sep. 2007.
- [7] B. Greaves, J. Collins, J. Parkes, and A. Tindal, "Temporal forecast uncertainty for ramp events," *Wind Eng.*, vol. 33, no. 4, pp. 309–319, Jun. 2009.
- [8] C. Ferreira, J. Gama, V. Miranda, and A. Botterud, "Probabilistic ramp detection and forecasting for wind power prediction," in *Reliability and Risk Evaluation of Wind Integrated Power Systems*. Springer, 2013, pp. 29–44.
- [9] J. W. Taylor, "Probabilistic forecasting of wind power ramp events using autoregressive logit models," *Eur. J. Oper. Res.*, vol. 259, no. 2, pp. 703–712, Jun. 2016.
- [10] Y. Li, P. Musilek, E. Lozowski, C. Dai, T. Wang, and Z. Lu, "Temporal uncertainty of wind ramp predictions using probabilistic forecasting technique," in *2016 IEEE Second International Conference on Big Data Computing Service and Applications (BigDataService)*, Oxford, UK, 2016, pp. 166–173.
- [11] P. Pinson, H. Madsen, H. A. Nielsen, G. Papaefthymiou, and B. Klöckl, "From probabilistic forecasts to statistical scenarios of short-term wind power production," *Wind Energy*, vol. 12, no. 1, pp. 51–62, 2009.
- [12] P. Pinson and R. Girard, "Evaluating the quality of scenarios of short-term wind power generation," *Appl. Energy*, vol. 96, pp. 12–20, 2012.
- [13] X. Ma, Y. Sun, and H. Fang, "Scenario generation of wind power based on statistical uncertainty and variability," *IEEE Trans. Sustain. Energy*, vol. 4, no. 4, pp. 894–904, Oct. 2013.
- [14] D. Ke, C. Chung, and Y. Sun, "A novel probabilistic optimal power flow model with uncertain wind power generation described by customized Gaussian mixture model," *IEEE Trans. Sustain. Energy*, vol. 7, no. 1, pp. 200–212, Jan. 2016.
- [15] G. Valverde, A. Saric, and V. Terzija, "Probabilistic load flow with non-Gaussian correlated random variables using Gaussian mixture models," *IET Gener. Transm. Distrib.*, vol. 6, no. 7, pp. 701–709, 2012.
- [16] R. Singh, B. C. Pal, and R. A. Jabr, "Statistical representation of distribution system loads using Gaussian mixture model," *IEEE Trans. Power Syst.*, vol. 25, no. 1, pp. 29–37, Feb. 2010.
- [17] I. González-Aparicio and A. Zucker, "Impact of wind power uncertainty forecasting on the market integration of wind energy in Spain," *Appl. Energy*, vol. 159, pp. 334–349, 2015.
- [18] S. Tewari, C. J. Geyer, and N. Mohan, "A statistical model for wind power forecast error and its application to the estimation of penalties in liberalized markets," *IEEE Trans. Power Syst.*, vol. 26, no. 4, pp. 2031–2039, 2011.
- [19] M. Cui, C. Feng, Z. Wang, J. Zhang, Q. Wang, A. R. Florita, V. Krishnan, and B.-M. Hodge, "Probabilistic wind power ramp forecasting based on a scenario generation method," in *Proc. IEEE Power Energy Soc. Gen. Meeting*, Chicago, IL, USA, 2017, pp. 1–5.
- [20] J. J. Moré and D. C. Sorenson, "Computing a trust region step," *SIAM J. Sci. Statist. Comput.*, vol. 4, no. 3, pp. 553–572, 1983.
- [21] J. Nocedal and Y. Yuan, "Combining trust region and line search techniques," in *Applied Optimization*. Springer US, 1998, pp. 153–175. [Online]. Available: https://doi.org/10.1007/2F978-1-4613-3335-7_7
- [22] S. Saks, *Theory of the Integral*. Courier Corporation, 1947.
- [23] P. Glasserman, *Monte Carlo Methods in Financial Engineering*. New York, NY, USA: Springer, 2003.
- [24] Y. Fu, M. Liu, and L. Li, "Multiobjective stochastic economic dispatch with variable wind generation using scenario-based decomposition and asynchronous block iteration," *IEEE Trans. Sustain. Energy*, vol. 7, no. 1, pp. 139–149, Jan. 2016.
- [25] W. T. Shaw, "Sampling Student's t distribution – use of the inverse cumulative distribution function," *J. Comput. Financ.*, vol. 9, no. 4, pp. 37–73, 2006.
- [26] The Mathworks, Inc. Statistics and Machine Learning Toolbox Functions. [Online]. Available: <https://www.mathworks.com/help/stats/mvnrnd.html>
- [27] M. Cui, J. Zhang, A. R. Florita, B.-M. Hodge, D. Ke, and Y. Sun, "An optimized swinging door algorithm for identifying wind ramping events," *IEEE Trans. Sustain. Energy*, vol. 7, no. 1, pp. 150–162, Jan. 2016.
- [28] J. Zhang, M. Cui, B.-M. Hodge, A. Florita, and J. Freedman, "Ramp forecasting performance from improved short-term wind power forecasting over multiple spatial and temporal scales," *Energy*, vol. 122, pp. 528–541, Mar. 2017.
- [29] C. Kamath, "Associating weather conditions with ramp events in wind power generation," in *Proc. Power Syst. Conf. Expo. (PSCE)*, Phoenix, AZ, USA, 2011, pp. 1–8.
- [30] C. Wan, Z. Xu, P. Pinson, Z. Y. Dong, and K. P. Wong, "Probabilistic forecasting of wind power generation using extreme learning machine," *IEEE Trans. Power Syst.*, vol. 29, no. 3, pp. 1033–1044, May 2014.
- [31] C. Gallego-Castillo, R. Bessa, L. Cavalcante, and O. Lopez-Garcia, "On-line quantile regression in the RKHS (Reproducing Kernel Hilbert Space) for operational probabilistic forecasting of wind power," *Energy*, vol. 113, pp. 355–365, Oct. 2016.
- [32] C. Feng, M. Cui, B.-M. Hodge, and J. Zhang, "A data-driven multi-model methodology with deep feature selection for short-term wind forecasting," *Appl. Energy*, vol. 190, pp. 1245–1257, 2017.
- [33] C. Draxl, A. Clifton, B.-M. Hodge, and J. McCaa, "The wind integration national dataset (WIND) Toolkit," *Appl. Energy*, vol. 151, pp. 355–366, Aug. 2015.
- [34] The Mathworks, Inc. Statistics Toolbox User's Guide. [Online]. Available: https://www.mathworks.com/help/pdf_doc/stats/stats.pdf
- [35] The Mathworks, Inc. Statistics and Machine Learning Toolbox. [Online]. Available: <https://www.mathworks.com/help/stats/fitgmdist.html>
- [36] The Mathworks, Inc. Generalized Extreme Value Distribution. [Online]. Available: <https://www.mathworks.com/help/stats/generalized-extreme-value-distribution.html>
- [37] Beaufort Scales (Wind Speed). [Online]. Available: <https://www.unc.edu/~rowlett/units/scales/beaufort.html>
- [38] K. Bruninx and E. Delarue, "A statistical description of the error on wind power forecasts for probabilistic reserve sizing," *IEEE Trans. Sustain. Energy*, vol. 5, no. 3, pp. 995–1002, Jul. 2014.
- [39] P. Pinson, "Estimation of the uncertainty in wind power forecasting," Ph.D. dissertation, Ecole des Mines de Paris, Paris, France, 2006.
- [40] W. Lin, J. Wen, S. Cheng, and W.-J. Lee, "An investigation on the active power variations of wind farms," *IEEE Trans. Ind. Appl.*, vol. 48, no. 3, pp. 1087–1094, May 2011.
- [41] M. Khodayar, H. Wu, S. D. Manshadi, and J. Lin, "Multiple period ramping processes in day-ahead electricity markets," *IEEE Trans. Sustain. Energy*, vol. 7, no. 4, pp. 1634–1645, Oct. 2016.
- [42] M. Cui, J. Zhang, H. Wu, and B.-M. Hodge, "Wind-friendly flexible ramping product design in multi-timescale power system operations," *IEEE Trans. Sustain. Energy*, vol. 8, no. 3, pp. 1064–1075, Jul. 2017.



Mingjian Cui (S'12-M'16) received the B.S. and Ph.D. degrees from Wuhan University, Wuhan, China, all in Electrical Engineering and Automation, in 2010 and 2015, respectively.

Currently, he is a Research Associate as a Postdoctoral at the University of Texas at Dallas. He was also a Visiting Scholar from 2014 to 2015 in the Transmission and Grid Integration Group (TGIG) at the National Renewable Energy Laboratory (NREL), Golden, CO. His research interests include power system operation, wind and solar forecasts, machine learning, data analytics, and statistics.



Jie Zhang (M'13-SM'15) received the B.S. and M.S. degree in Mechanical Engineering in 2006 and 2008, respectively, both from Huazhong University of Science & Technology, Wuhan, China and the Ph.D. degree in Mechanical Engineering from Rensselaer Polytechnic Institute, Troy, NY, in 2012.

He is currently an Assistant Professor in the Department of Mechanical Engineering at the University of Texas at Dallas. His research interests include multidisciplinary design optimization, complex engineered systems, big data analytics, wind and solar forecasting, renewable integration, energy systems modeling and simulation.



Qin Wang (M'10) received the B.S. degree in the Department of Electrical and Electronics Engineering from Huazhong University of Science & Technology, Wuhan, China, in 2006, the M.S. degree in Electrical Engineering from South China University of Technology, Guangzhou, China, in 2009, and the Ph.D. degree in the Electrical and Computer Engineering Department at Iowa State University, Ames, IA, in 2013.

He is currently working at the National Renewable Energy Laboratory in Golden, Colorado. His previous industry experiences include internships at ISO New England and a full-time position at Midcontinent ISO. His research interests include power system reliability and online security analysis, smart distribution systems, transactive energy, transmission planning, and electricity markets.



Venkat Krishnan (M'15) received the M.S. and Ph.D. degrees from Iowa State University (ISU), Ames, IA, USA, in 2007 and 2010, respectively. His research interests include electricity system capacity expansion planning, power transmission and distribution systems stability and security assessments, markets, and energy storage integration.

He is currently a Senior Engineer in the Power System Design and Studies (PSDS) group at the Power System Engineering Center (PSEC) in National Renewable Energy Laboratory (NREL), Golden, CO, USA.



Bri-Mathias Hodge (M'10-SM'17) received the B.S. degree in chemical engineering from Carnegie Mellon University in 2004, the M.S. degree from the Process Design and Systems Engineering Laboratory of Åbo Akademi, Turku, Finland, in 2005, and the Ph.D. degree in chemical engineering from Purdue University in 2010.

He is currently the Manager of the Power System Design and Studies Group at the National Renewable Energy Laboratory (NREL), Golden, CO. His current research interests include energy systems modeling, simulation, optimization, and wind power forecasting.